Using pH dependence to understand mechanisms in electrochemical CO reduction

Georg Kastlunger[a], Lei Wang[b,c], Nitish Govindarajan[a], Hendrik H. Heenen[a], Stefan Ringe[d,e], Thomas Jaramillo[b], Christopher Hahn[f,g], Karen Chan[a],*

[a]Catalysis Theory Center, Department of Physics, Technical University of Denmark (DTU), 2800 Kgs. Lyngby, Denmark

[b]SUNCAT Center for Interface Science and Catalysis, Department of Chemical Engineering, Stanford University, Stanford, CA 94305, USA

[c]Department of Chemical and Biomolecular Engineering, National University of Singapore, Singapore 117585, Singapore

[d]Department of Energy Science and Engineering, Daegu Gyeongbuk Institute of Science and Technology, Daegu, Republic of Korea

Energy Science and Engineering Research Center, Daegu Gyeongbuk Institute of Science and Technology (DGIST), Daegu 42988, Republic of Korea

[f]SUNCAT Center for Interface Science and Catalysis, SLAC National Accelerator Laboratory, Menlo Park, CA 94025, USA

[g]Materials Science Division, Lawrence Livermore National Laboratory, Livermore, CA 94550, USA

ABSTRACT

Electrochemical conversion of $CO_{(2)}$ into hydrocarbons and oxygenates is envisioned as a promising path towards closing the carbon cycle in modern technology. To this day, however, the reaction mechanisms towards the plethora of products are disputed, complicating the search for novel catalyst materials. In order to conclusively identify the rate-limiting steps in CO reduction on Cu, we analyzed the mechanisms on the basis of constant potential DFT kinetics and experiments at a wide range of pH values (3 - 13). We find that *CO dimerization is energetically favoured as the rate limiting step towards multi-carbon products. This finding is consistent with our experiments, where the reaction rate is nearly unchanged on an SHE potential scale, even under acidic conditions. For methane, both theory and experiments indicate a change in the rate-limiting

step with electrolyte pH from the first protonation step in acidic/neutral conditions to a later one in alkaline conditions. We also show, through a detailed analysis of the microkinetics, that a surface combination of *CO and *H is inconsistent with the measured current densities and Tafel slopes. Finally, we discuss the implications of our understanding for future mechanistic studies and catalyst design.
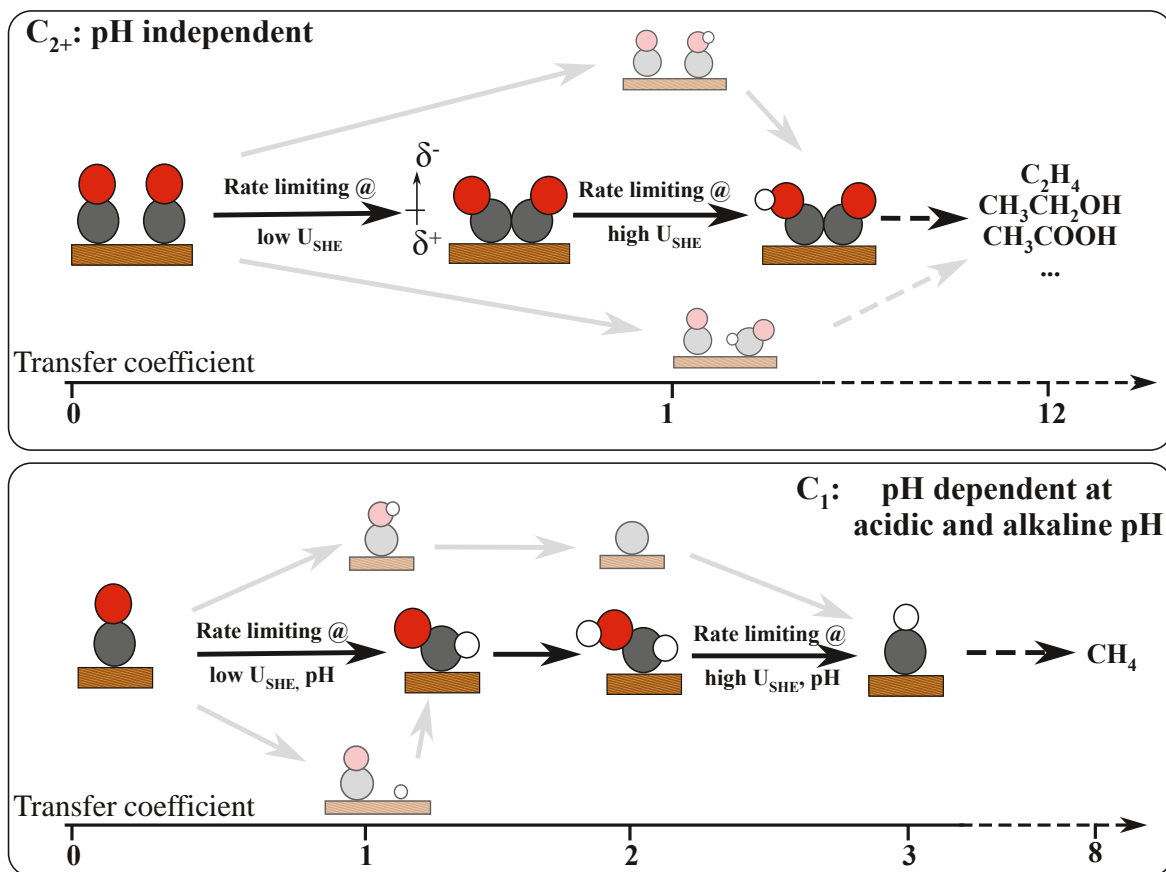

Table of contents figure

INTRODUCTION

The impact of fossil fuel consumption on earth's environment and climate necessitates sustainable alternatives in the production, storage and use of energy resources[1,2]. Electrocatalysis is a means to convert renewable electric power to chemicals, which are an ideal medium for long-term storage and potential building blocks for the chemical industry[1]. Electrochemical $CO_{(2)}$ reduction ($eCO_{(2)}R$) represents a prime candidate for this task, since it directly closes the industrial carbon cycle by using one of the major greenhouse gases as its input and converting it into high value fuels and chemicals[1–3]. However, the process suffers from major limitations due to the energy demand associated with CO_2 capture [4–6], energy losses from large overpotentials[2] for the catalysis towards valuable multi-carbon (C_{2+}) products and the cost of separating and purifying the variety of products[7]. Furthermore, to this day, C_{2+} products can only be produced on Copper (Cu) based electrodes with reasonable selectivity, and despite decade-long $eCO_{(2)}R$ research[3,8,9], the associated catalytic mechanisms is still disputed. Without understanding of the crucial steps in the conversion of CO_2 towards the various products, the prediction of feasible catalyst alternatives on the basis of large-scale catalyst screening will remain based on trial and error.

Numerous attempts have been made in recent years to identify the rate-limiting steps in the reaction pathways for $eCO_{(2)}R$ on Cu electrodes [10–19]. Here, a crucial piece of the puzzle is provided by the fact that $eCO_{(2)}R$ towards C_{2+} products is pH independent on an absolute potential scale (e.g. the standard hydrogen electrode, SHE), as already shown in the seminal work of Hori et al.[8,9]. This observation vastly narrows down the possible elementary steps that can be rate-limiting in the production of C_{2+} products as it demands an early rate limiting step, as outlined in Figure 1.

Several studies have hypothesized the rate-limiting step in the production of C_{2+} products to be the first elementary step involving the dimerization of *CO to form the *OCCO species, which does not involve a proton transfer[12,20–23]. However, alternative mechanisms based on an initial proton-coupled electron transfer (PCET) to *CO followed by the coupling of reaction intermediates in the later steps of the reaction have also been proposed [24–28]. As we will show in detail, when we consider the reaction kinetics, we find that it is not possible to unequivocally exclude the involvement of a proton transfer in an initial rate-limiting step without activity studies with sufficient concentration of proton donors other than H_2O, e.g. hydronium (H_3O^+) in acidic conditions or buffering anions[19,29]. Hence, four possible RLS satisfy the experimentally observed pH independence, as outlined in the upper panel of Figure 1: (1) the coupling of 2 *CO molecules to form the *OCCO dimer species[12,21–23], (2) the protonation of the *OCCO dimer to *OCCOH[19], and the rate-limiting protonation of *CO to (3) *COH or (4) *CHO followed by C-C coupling in a later elementary step along the reaction pathway[24–28]. This assignment of the possible RLS being an initial step in the reaction network is supported by the reported high Tafel slopes[19,30,31], being the change in overpotential necessary for an order of magnitude change in current density, towards C_{2+} products in alkaline conditions.

Similarly, the $eCO_{(2)}R$ reaction mechanism towards methane (CH_4) has been investigated in several theoretical[10,14,32–36] and experimental studies[8,30,37–42]. The experimental studies show a reduction in the CH_4 partial current density at a given electrode potential on the SHE scale with increasing electrolyte pH (i.e. it is pH dependent). This observation suggests that the mechanism for CH_4 production deviates substantially from the C_{2+} pathway with an elementary step beyond the first protonation reaction being rate limiting. The challenge for this reaction lies in identifying the actual reaction pathway, given the various possibilities that exist even in the early stages of the mechanism, as outlined in the lower panel of Figure 1 (C_1 pathways). In addition to routes to CH_4

only involving PCETs, the possibility of surface hydrogenation of *CO following a Langmuir-Hinshelwood type mechanism has also been proposed in recent studies [43,44]. Overall, there are many possibilities for the mechanism of $eCO_{(2)}R$ towards the various products and the actual pathways towards the various products need to be narrowed down in order to enable the search for improved electrocatalysts in e.g. theoretical screening studies.
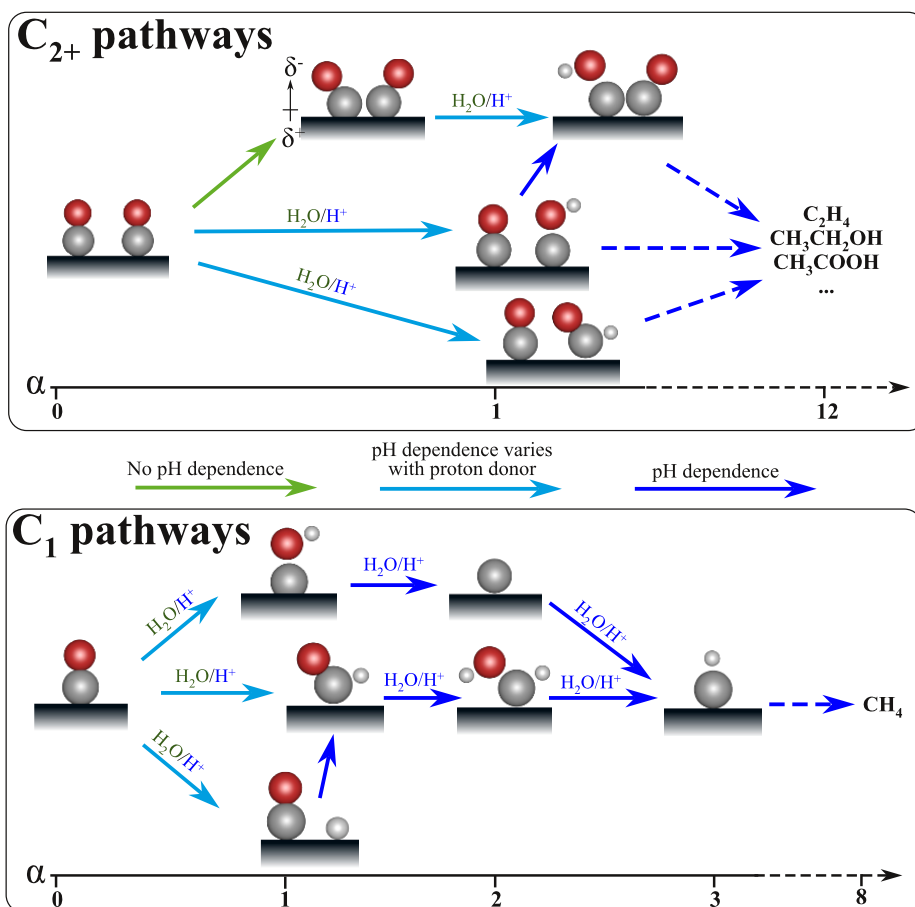

Figure 1: Schematic of the possible reaction mechanisms towards the production of C_{2+} products and CH_4 during electrochemical CO reduction on Cu. The colors of the arrows indicate the varying pH dependence in the case of the respective step being the rate-limiting step of the reaction. Note that the charge transfer coefficient (α) can deviate from integer values for the reaction intermediates as a consequence of the non-zero surface dipole, as discussed in detail in the text.

In this article, we present a joint theoretical and experimental study to identify the rate-limiting steps towards C_{2+} products and CH_4 by investigating the effect of the electrolyte pH during electrochemical CO reduction (COR) on Cu electrodes. For this, we construct elaborate microkinetic models based on the reaction kinetics determined from grand-canonical (constant potential) DFT calculations[45], accounting for both H_2O and H_3O^+ as proton donors, and considering a series of representative surface facets. We identify that the dimerization of *CO is favored over its initial protonation to *COH/*CHO at all investigated pH's, and the potential response of *CO dimerization alone can explain the experimentally observed Tafel slopes, as a

4

direct consequence of the large degree of polarization of the *OCCO dimer species. In contrast to the observations for C_{2+} products, we identify a change in the rate-limiting step with a change in the electrolyte pH and proton donor in the COR reaction pathway towards CH_4. The mechanism exhibits pH dependent activity in acidic conditions (H_3O^+ as proton donor) and for high pH values a. This behavior is a consequence of a change in the rate-limiting step from the first PCET step to the third PCET step with increasing electrolyte pH as we find in our *ab-initio* kinetics studies on the reaction pathway. Based on a series of qualitative disagreements with experimental observations, we exclude surface hydrogenation in the reaction mechanism towards CH_4. We validate our theoretical findings via pH-dependent measurements under acidic (pH 3), neutral (pH 7) and alkaline (pH 13) conditions, which allows us to directly distinguish between the involvement of a PCET vs. the dimerization of *CO in the rate-limiting step of COR towards C_{2+} products. We find that, even at pH 3, where there is sufficient concentration of H_3O^+ and/or buffer species to be viable proton donor(s), the measured current densities towards C_{2+} products are independent of the electrolyte pH on an SHE scale, confirming that a proton transfer is not involved in the rate-limiting step of the reaction pathway. On the other hand, our measurements on the activity towards methane show a clear decrease with increasing electrolyte pH, while substantially increasing its Tafel slope, in line with the theoretical assessment.

Our manuscript is structured as follows: We first give an overview of the features of generic Tafel plots (current density at a range of applied potentials) associated with multi-step reduction reactions with water (H_2O) and hydronium ions (H_3O^+) as proton donors. Next, we discuss the reaction mechanisms for COR on the basis of our potential-dependent *ab-initio* kinetics[45], where we highlight the competition of *CO dimerization and an initial protonation of *CO for the mechanism towards C2+ products, as well as, the competition of a purely PCET based and surface hydrogenation based mechanism towards CH_4. Then we compare the theoretical results with our measured activities and a collection of literature $eCO_{(2)}R$ datasets.

We believe that the in-depth mechanistic study of the reaction mechanism of $CO_{(2)}R$ and the effects of electrolyte pH on multi-step electrochemical reactions presented in this work will provide important descriptors and guidelines for the search for improved Cu-catalyst morphologies or alternatives to Cu in catalyst screening studies for the production of electrofuels.

THEORETICAL BACKGROUND

The Tafel slopes and pH-dependence of multi-step reduction reactions

In order to set a qualitative basis for performing our mechanistic analysis on the reaction pathways of COR, Figure 2 shows the effects of pH and U_{SHE} on Tafel plots for reduction reactions. In the top panel (I), we consider three types of single elementary steps. We show the variations in the corresponding current density (j) with respect to variations in both pH and U_{SHE}. We consider three possibilities: (i) a potential sensitive chemical reaction (as exemplified by the *CO dimerization step), and PCET steps in (ii) neutral/alkaline and (iii) acidic conditions. In case (i), the electrolyte pH has no effect on j (vs U_{SHE}), since H_3O^+/OH^- species are not involved in the elementary step. Similarly, if H_2O were a proton donor in a PCET step (case ii), the chemical potential of H_3O^+ or OH^- has no effect on the initial or transition states and, therefore, pH has no effect on the measured current densities. However, as we will show in panel II and III below, since the final state of the reaction is dependent on pH via the activity of OH^-, any rate limiting step following an elementary step of case (ii) would lead to pH dependence, in contrast to case (i). Finally, if H_3O^+ is the proton donor in a PCET step (case iii), its activity affects the free energy of
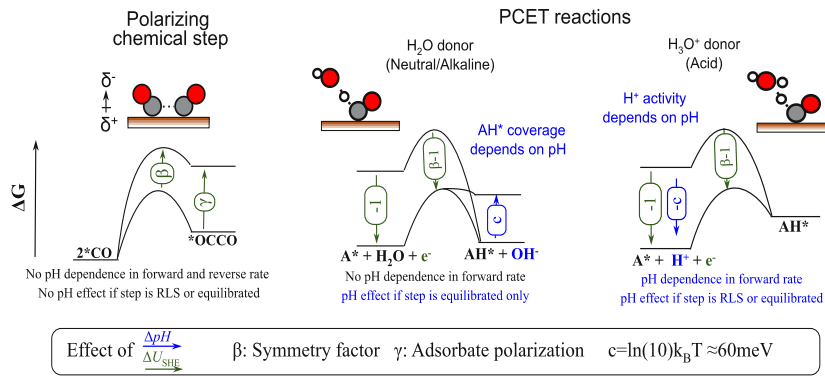
5

the initial state and therefore corresponding activation energy, such that the rate (and measured j) decreases with increasing pH.

The pH dependence of the elementary steps extends to multi-step reactions, as illustrated in Panels (II) and (III) of Figure 2. These panels show the pH and U_{SHE} dependences corresponding to generic mechanisms with multiple PCETs (Panel III a) and with an initial potential sensitive surface reaction, followed by PCETs (Panel III b). The left and right sides of these panels show the cases where H_2O and H_3O^+ are the proton donor, respectively. In panel II, we also show the corresponding generic free energy diagram including a sequence of elementary steps. Here, note that both a decrease in U_{SHE} and pH can shift the rate limiting step (RLS, indicated by the point on the FED with highest free energy) from a later to an earlier elementary step. These shifts in RLS give rise to increasing Tafel slopes with decreasing U_{SHE}, as illustrated in the Tafel plots in panel III. At high overpotentials (regions of the most negative U_{SHE}), the RLS shifts to the first elementary step, which results in the pH dependence shown in panel I. At lower overpotentials (more positive U_{SHE}), the RLS shift to the second step. Consider the left side of panel III(a): Here, even though H_2O is the proton donor, there is a dependence of j on pH. This pH dependence arises from the pH-dependence (a Nernstian shift) in the coverage of the intermediate involved in the RLS. It persists until the RLS shifts to the first step due to an increase in overpotential or a saturation of the intermediate's coverage, e.g. if the formation of the intermediate is exergonic, the pH dependence disappears.
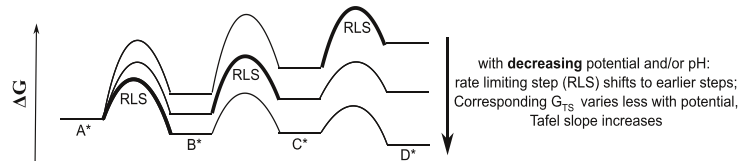
When H_3O^+ is the proton donor (cf. right side of Panel I and III in Fig. 2), its activity affects the free energy of the first elementary step, as well as the RLS, thus leads to twice the effect of pH on j, compared to H_2O as the proton donor. In the case of a multi-step mechanism consisting of a polarizing chemical step followed by PCETs (Panel III b), the pH dependence manifests at potential ranges where the RLS is located after or at the first PCET for the cases where H_2O and H_3O^+ are the proton donors, respectively.

Note that we did not explicitly consider the impact of buffers in Figure 2. Buffers may act as proton donors directly or alter the pH[46]. If either of these two scenarios are at play, there would be a difference in activity (on the SHE scale) vs. the case where H_2O is the proton donor and a dependence on the buffer concentration might be observed analogue to the concentration of H_3O+ and pH.

I. pH dependence of elementary steps

Effect of $\dfrac{\Delta pH}{\Delta U_{SHE}}$ β: Symmetry factor   γ: Adsorbate polarization $c=\ln(10)k_BT \approx 60meV$

II. Energetics of multistep reductions

with **decreasing** potential and/or pH:
rate limiting step (RLS) shifts to earlier steps;
Corresponding G_{TS} varies less with potential,
Tafel slope increases

III. Currents of multistep reductions

(a) PCETs only

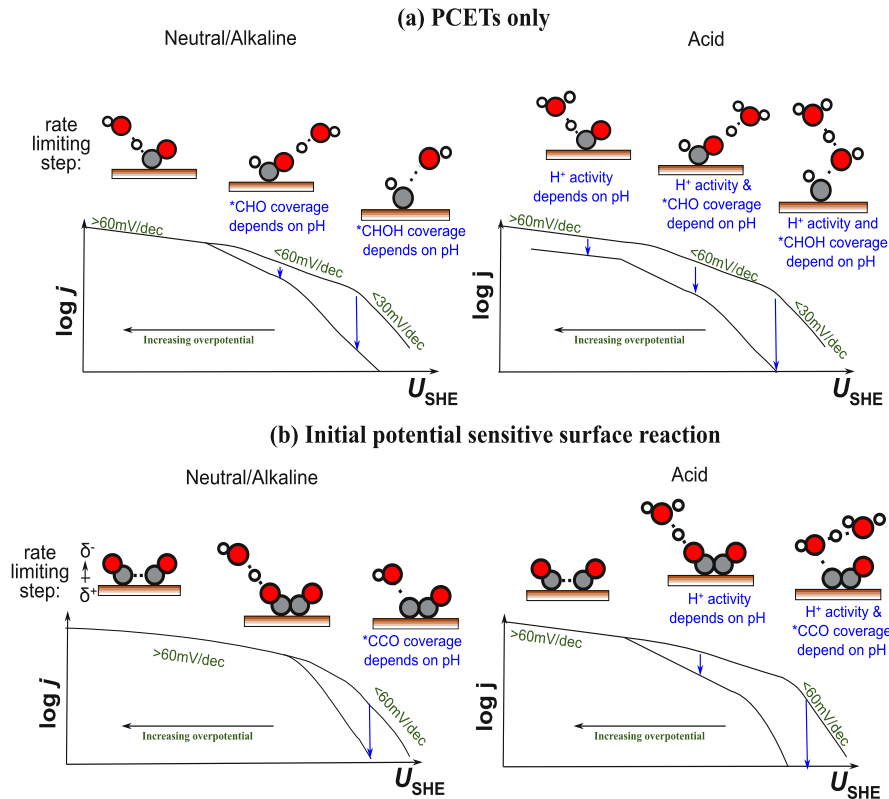

(b) Initial potential sensitive surface reaction

Figure 2: Schematic illustration of the influence of the potential, U_{SHE} (green) and electrolyte pH (blue) on the reaction energetics and measured current densities of elementary steps (panel I) and multistep reaction processes (Panels II and III). In addition to the qualitative behavior, panel I

shows the quantitative changes in free energy with potential (green arrows) and pH (blue arrows) given as the coefficients to ΔU_{SHE} and ΔpH. Panel II, the extension of panel I to multistep reactions, emphasizes the qualitative influence of U_{SHE} and pH on the reaction energetics and the RLS. In panel III, the qualitative pH dependence of the current density and changes in the Tafel slope upon varying the potential are depicted. Here, we distinguish between a pure PCET driven process (panel III a) and a process including a potential sensitive surface reaction (panel III b). The respective RLS at a given U_{SHE} is given in the illustrations above the qualitative polarization curves.

Let us now put the described behavior into a more complete thermodynamic framework. In general, the dependence of electrochemical reactions on the applied potential U and pH follows an Arrhenius-like behavior,

$$r(U,pH) = k_0 \exp\left(-\frac{\Delta G^{\ddagger}(U,pH)}{k_B T}\right), \qquad (1)$$

where $r(U,pH)$ is the rate of the reaction, k_0 refers to the product of the prefactor ($\frac{k_B T}{h}$) and the concentration of the reactants in the chosen standard state (denoted by the subscript 0), T refers to the temperature and k_B represents the Boltzmann constant. $\Delta G^{\ddagger}(U,pH)$ represents the effective activation free energy of the reaction and may be dependent on the applied potential, the pH, activities of reactants, as well as temperature and pressure. Given the exponential dependence of the current on $\Delta G^{\ddagger}$, we usually work with the rate on a logarithmic scale:

$$\log_{10} r = \log_{10} k_0 - \frac{\Delta G^{\ddagger}(U,pH)}{\ln(10)k_B T}. \qquad (2)$$

All the quantities defining $\log_{10} r$ are constants with respect to pH and potential except for $\Delta G^{\ddagger}$. Hence, the major responsible for the Tafel slope is the dependence of $\Delta G^{\ddagger}$ on U. However, the pH has an indirect influence on it as well by e.g. changing the rate-limiting step and the proton donor along the reaction pathway.

Based on the chosen potential scale, varying definitions can be applied for $\Delta G^{\ddagger}$. On a purely electronic scale (e.g. SHE), $\Delta G^{\ddagger}$ can be defined by combining the thermodynamic contributions up to the RLS and the activation free energy of the RLS:

$$\Delta G^{\ddagger} = \underbrace{\sum^{N_H} \Delta G_{0,i} - N_H(\mu_e + \mu_p) - \gamma\mu_e}_{Thermodynamics} \;\; + \;\; \underbrace{\Delta G_{0,RLS}^{\ddagger} - \beta\mu_e - \mathbf{\mu_p}}_{Kinetics}. \quad (3)$$

Here, $\Delta G_{0,i}$ and $\Delta G_{0,RLS}^{\ddagger}$ refer to the free energy of reaction of the N_H PCET reactions i up to the RLS and the reaction barrier of the RLS, respectively, where the subscript 0 refers to a well-defined electrochemical standard state which we choose as $U = 0 V_{SHE}$ and pH = 0. The electronic effect on $\Delta G^{\ddagger}$, which arises from the applied potential, is included in the chemical potential of the electrons with respect to this reference state $\mu_e = -eU_{SHE}$, and the effect of pH arises from the (entropic) change of the chemical potential of the reacting protons (H_3O^+,p) and hydroxide ions (OH^-) $\mu_p = -\mu_{OH} = -\ln(10)k_B TpH$ with the electrolyte pH with respect to pH=0 (Note that although μ_e and μ_p are changes in chemical potential with respect to the standard state, we omitted the Δ for clarity). Both the electronic and proton chemical potentials contribute nearly equally to the *thermodynamics*, which lead to the huge success of the computational hydrogen electrode (CHE) model[47]. The influence of μ_p on *kinetics*, on the other hand is only present in acidic

conditions, as indicated again in Eq. (3) by the light blue color and shown in the top panel of Figure 2, since only in such a case the proton is a reactant in the RLS.

Three coefficients in equation (3) determine the magnitude of the influence of a change in potential and pH on $\Delta G^{\ddagger}$: N_H: the number of proton transfers from the electrolyte (or PCET steps) preceding the RLS; γ: the energetic response to the overpotential of the reactants in the RLS, arising from the induced dipole perpendicular to the electrode surface[48], and β: the symmetry factor of the RLS.[49] Depending on the nature of the rate-limiting step, various combinations of N_H, γ and β exist, which affect the Tafel plots differently. We highlight three characteristic limits of these coefficients on an SHE scale below:

$N_H = 0$: No proton transfer precedes the RLS, Tafel slope> 60 mV/dec (for any $1 > \beta > 0$), pH dependence appears only when H_3O^+ is the proton donor (i.e. in acidic conditions). An example is the formation of CO from CO_2 on Au, where the potential sensitive adsorption of CO_2 has been found to be rate limiting[29].

$\gamma \approx 0$: Reactants in RLS do not alter the surface dipole compared to the bare slab. In this case only PCET steps contribute to the Tafel slope. HER is an example here, given the negligible surface dipole of $*H$[50].

$\beta \approx 0$: RLS is non-electrochemical (including virtually no change to the surface dipole), and coverages dictate the potential response. An example is the Tafel reaction of HER[50].

We can now rewrite equation 3 by splitting the pH and potential effects (and replacing μ_e, μ_p):

$$\Delta G^{\ddagger} = \sum^{N_H} \Delta G_{0,i} + \Delta G^{\ddagger}_{0,RLS} + (N_H + \gamma + \beta)U_{SHE} + (N_H + 1)\ln(10)\, k_B TpH \qquad (4)$$

Where we again highlight the pH effect only present in the acidic case (i.e. where H_3O^+ is a reactant) by a light blue color. The three contributions to the effect of the overpotential on $\Delta G^{\ddagger}$ in equation 4 are captured by the transfer coefficient $\alpha = N_H + \gamma + \beta$. α, therefore, incorporates the net potential dependence and defines the measured Tafel slopes as

$$\left(\frac{\partial \log_{10} r}{\partial U}\right)^{-1}_{pH} = \left(\frac{\partial \log_{10} r}{\partial \Delta G^{\ddagger}}\frac{\partial \Delta G^{\ddagger}}{\partial U}\right)^{-1}_{pH} = -\frac{\ln(10)k_B T}{e\alpha}. \qquad (5)$$

While N_H is an integer, both γ and β can add up continuously along the reaction pathway. Hence, α is a smooth function meaning that the resulting Tafel slopes are not limited to any characteristic ("cardinal") values such as 60 or 120mV/dec, as has also been highlighted in a recent statistical study on experimentally determined Tafel slopes[51].

Equation 4 also shows how N_H influences the pH dependence of $\Delta G^{\ddagger}$, while γ and β only affect the potential dependence:

$$\left(\frac{\partial \log_{10} r}{\partial pH}\right)_{U_{SHE}} = \left(\frac{\partial \log_{10} r}{\partial \Delta G^{\ddagger}}\frac{\partial \Delta G^{\ddagger}}{\partial pH}\right)_{U_{SHE}} = -(N_H + 1). \qquad (6)$$

Hence, the pH dependence is only affected by the number of proton transfers (N_H) before the RLS and the nature of the proton donor. In the case where H_3O^+ is the proton donor (acidic conditions), the pH effect is always increased by a factor of one with respect to the case where

H₂O is the proton donor (in neutral/alkaline conditions), as indicated by the light blue color in equation (6). As a rule, for electrochemical reduction reactions, without considering specific double layer effects, the only possible effect of increasing pH at a given applied potential on an absolute potential scale (e.g. SHE) is a reduction in the current density j, since $N_H \geq 0$.

Finally, on the reversible hydrogen electrode (RHE) scale, changes in μ_p are countered by an equal and opposite change in μ_e, thus keeping the total electrochemical driving force $\mu_{pe} = \mu_e + \mu_p = -eU_{RHE} = -(eU_{SHE} + 2.3k_BTpH)$ constant. As a consequence, the potential and pH effects cannot be separated anymore. While we discuss the energetics on this potential scale in more detail in section 9 of the SI, we highlight here that, on an RHE scale, an increase in the electrolyte pH can, for a reduction process, lead to both an increase (in neutral/alkaline conditions) or a decrease (in acidic conditions) of the reaction rate.

RESULTS AND DISCUSSION

DFT simulations and kinetic modelling suggest the formation of C₂₊ products through CO dimerization is favored over a later coupling step

In order to assess the competition of the initial elementary steps exhibiting pH independence towards C₂₊ products, we simulated constant-potential kinetics with DFT applying the solvated jellium method (SJM) [52] with H₂O as the proton donor (see SI for computational details). Figure 3(a) shows the resulting free energy diagrams for *CO dimerization, as well as, the protonation of *CO to *COH or *CHO followed by the coupling to *CO to form *OCCOH/*OCCHO on Cu(100). The 100 facet was chosen based on our finding that CO dimerization is significantly more facile on this facet compared to the 111 terrace and 211 steps and is comparable to the coupling on the 110 facet (see section 3 of the SI). We find that the *CO dimerization step followed by the protonation of *OCCO is kinetically favored over the initial protonation of *CO to *CHO/*COH. We attribute the smaller protonation barrier of *OCCO relative to *CO to the substantial polarization of the *OCCO species. The negative partial charge on the oxygen atoms greatly facilitates the protonation process.
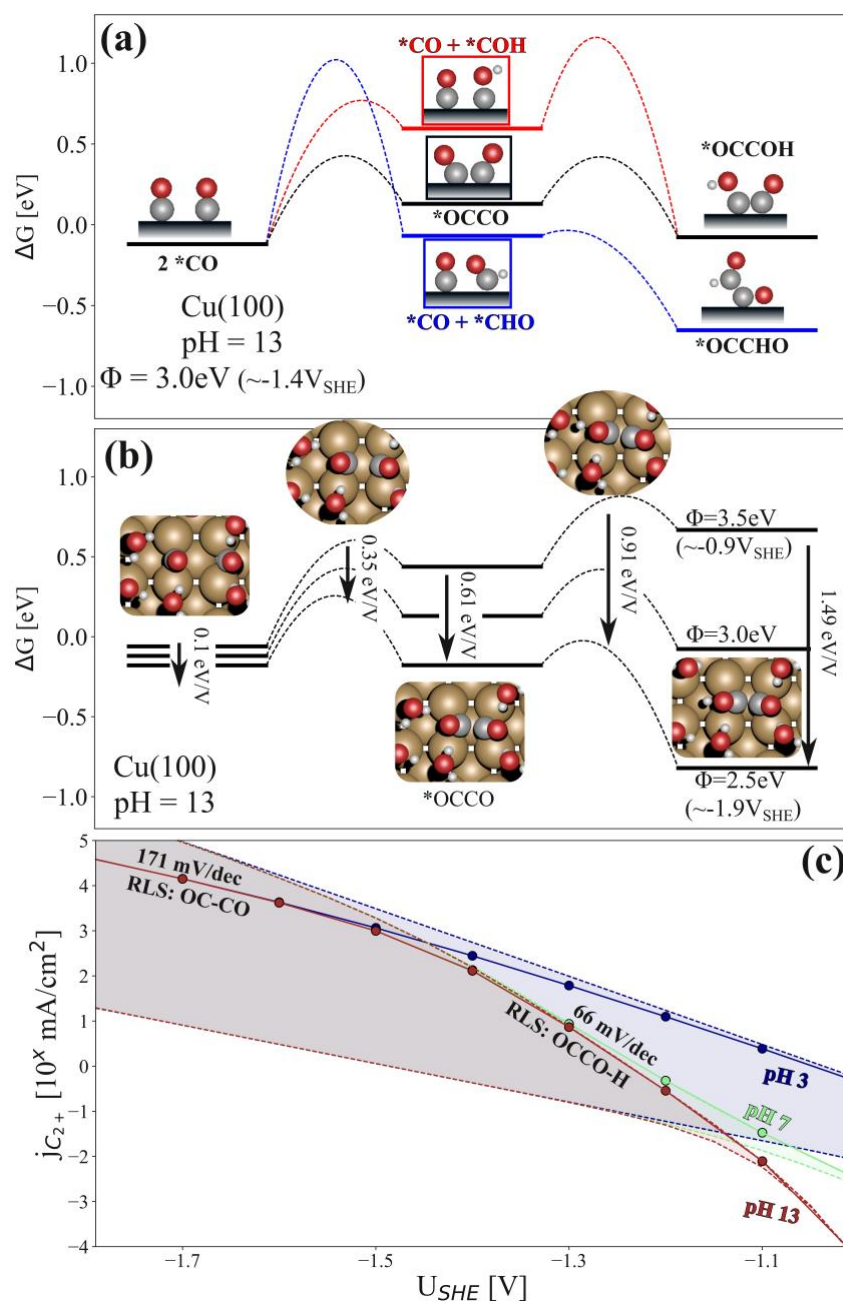
Figure 3: (a) DFT calculated free energies for initial C-C coupling pathways including *CO dimerization and the protonation of *CO to *COH/*CHO followed by coupling with *CO. In all reactions in this panel, H_2O was considered as the proton donor. (b) Potential dependence of the reaction energetics along the *CO dimerization pathway computed using constant potential DFT simulations on the 100 facet. The energy response to an increase in overpotential is highlighted by the arrows. (c) Simulated current densities resulting from a microkinetic model based on the DFT calculated energetics for Cu(100). A surface fraction of 19% [59] was used in the microkinetic model. The shaded areas correspond to error estimates associated with uncertainty in the CO dimerization barrier typical for DFT (+/- 0.2eV)[60]. At all shown pHs both hydronium and H_2O have been considered as proton donors and the transport limitation of protons has been regarded following

Ref. [61] In panels (a) and (b) full lines refer to thermodynamic stable states, while dashed lines represent transition state energies. The potential in both panels (a) and (b) are given in terms of the calculated work functions (ϕ). The translation from ϕ to U_{SHE} in panel (b) has been made using the following relation: $U_{SHE} = (\phi - 4.4 \text{ eV})/e$ [62]. Note that although only the first two elementary steps are shown here, in the microkinetic model in panel (c) more subsequent steps have been included as outlined in tables S1 and S2.

The finding that the Cu(100) and Cu(110) facets largely facilitate *CO dimerization is in line with previous theoretical[53] and experimental studies, where e.g. the application of Cu nanocubes[25,40,54,55], exhibiting predominantly 100 and 110 facets, and single crystals[9,20,56] are reported to be selective towards C_{2+} products. However, we emphasize that particular care in assigning active sites is needed, given that a reconstruction of the ideal surface under reaction conditions cannot be excluded and only a small fraction of more active sites can, in principle, dominate the kinetics of the reaction[57,58].

Figure 3(b) shows the potential dependence of the free energies of the reaction steps involved in the *CO dimerization pathway, and Figure 3(c) the simulated current densities from corresponding microkinetic models at various pH values. The computations suggest that at low overpotentials, *OCCOH formation would be rate limiting (i.e. the corresponding transition state energy is the highest point in the free energy diagram), while at lower (more reducing) potentials, the *CO dimerization step is the bottleneck towards C_{2+} products. This change in rate-limiting step is reflected in the increase in the simulated Tafel slope with more reducing potentials akin to the schematic in Figure 2 (panel III).

The transition state of *CO dimerization shows a potential dependence of 0.35 eV/V, as a consequence of the buildup of a surface dipole during the dimerization. This potential response translates into an effective transfer coefficient (α) of the same value, resulting in the computed Tafel slope of 171 mV/dec from equation 5. For the *OCCO intermediate, we found a stabilization (γ) of 0.61 eV/V with the applied potential. This response to the potential is also incorporated in the subsequent transition state for the protonation of *OCCO which we found to have a symmetry factor (β) of 0.3 eV/V and, hence, an overall stabilization ($\beta + \gamma$) of 0.91 eV/V. The corresponding Tafel slope for this protonation step is 66 mV/dec.

Using a microkinetic model[63], the calculated reaction energetics translate to the simulated current densities shown in Figure 3(c). For pH 7 and 13, where H_2O dominates as the proton donor, the protonation of *OCCO to *OCCOH is the RLS for $U < -1.4 V_{SHE}$. At increased overpotentials, the RLS changes to *CO dimerization with a concomitant increase in the Tafel slope. For pH 3, on the other hand, where H_3O^+ is the predominant proton donor, CO-CO dimerization is the RLS throughout the considered potential range, as a consequence of the spontaneous (activationless) protonation of *OCCO in our acidic transition state simulations.

In order to illustrate the sensitivity of the simulated current density and Tafel slopes, we also added error estimates in Figure 3(b), represented by the shaded regions. In these regions the *CO dimerization barrier was varied by +/- 0.2 eV. This analysis shows that an increase of the *CO dimerization barrier by 0.2 eV already leads to a three orders of magnitude reduction in the simulated current density towards C_{2+} products and a Tafel slope corresponding to the *CO dimerization step being rate-limiting throughout the experimentally investigated potential region. These observations highlight the sensitivity of the mechanism (and simulations in general) to the computed reaction energetics. Hence, we emphasize that the main finding from our theoretical analysis is that a C_2 pathway with C-C coupling through *CO dimerization is preferred over

pathways involving later coupling steps between protonated intermediates. Furthermore, the *CO dimerization step exhibits a significant potential response, consistent with the measured Tafel slopes.

Note that although Figure 3(a) and (b) only show the free energies of the first two elementary steps for clarity, in the microkinetic model of panel (c) more subsequent reaction barriers and thermodynamics up to the ketene intermediate (*H2CCO)[64] have been included, as outlined in tables S1 and S2. We also emphasize here that we have not considered buffer species as proton donors in our simulations, which would also lead to differences in activity at different pH (e.g. for the experiments at pH 3 and pH 7 which involve buffering anions), in the potential region where *OCCOH formation involving a proton transfer to the *OCCO dimer is the rate-limiting step.

DFT calculated energetics suggest a purely electrochemical mechanism towards CH₄

In contrast to C_{2+} products, a pH dependence in the mechanism to methane is generally observed in alkaline conditions[3,31]. Following the scheme in Figure 2(III), this suggests that a reaction step after the first PCET is of importance for this product. Hence, two fundamentally different reaction routes appear viable for methane production:

Mechanism-I: a purely *electrochemical* process consisting of an initial PCET to *CO to form *CHO/*COH, followed by the subsequent PCET steps towards CH₄ (cf. Figure 1). A later step in the pathway would be rate limiting ($N_H > 0$), which leads to a smaller Tafel slope and a distinct pH dependence. As suggested in the Figure 2(II) a smaller pH could give rise to a shift in the RLS to the first protonation step of *CO, where no pH dependence is expected ($N_H = 0$) except in the case of a change in proton donor that leads to a change in the activation energy $\Delta G^{\ddagger}_{0,RLS}$ for the proton transfer.

Mechanism-II: the *surface hydrogenation* of *CO is the rate-limiting step as has been discussed in previous studies [43,44]. Since surface hydrogenations are chemical processes that are largely insensitive to changes in the applied potential, a finite Tafel slope would arise from a change in *H coverage at high pH, which in the Nernstian limit would give rise to slopes close to 60 mV/dec and a distinct pH dependence.
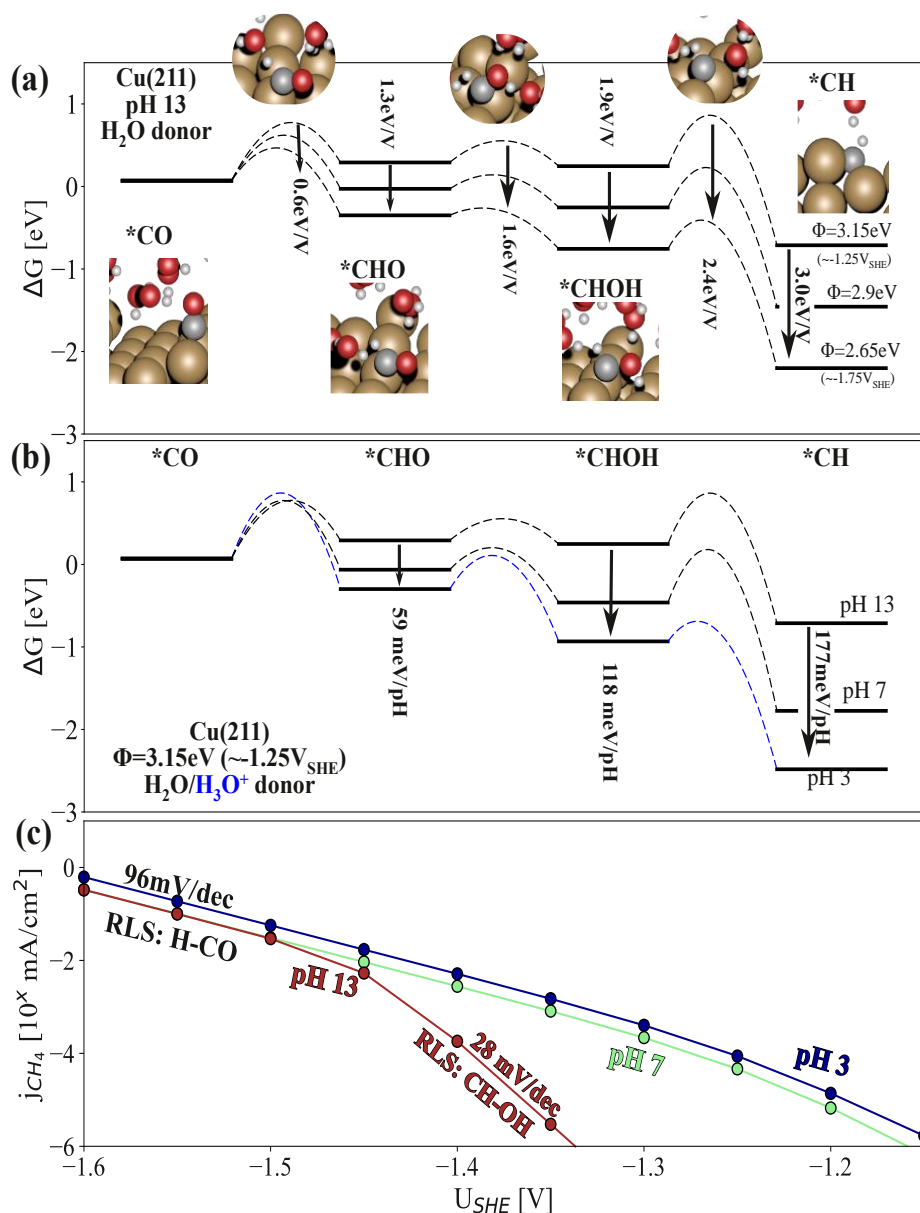
Figure 4: (a) Free energy diagram for Cu(211) towards CH$_4$ at varying workfunctions (a link to the experimental SHE potential scale can be made using the relation: $U_{SHE} = (\phi - 4.4 \text{ eV})/e$). (b) Free energy diagram for the reaction pathway towards CH$_4$ at varying electrolyte pH. For pH 7 and 13, the reaction kinetics are simulated with H$_2$O is the proton donor, while the kinetic simulations at pH 3 were performed with H$_3$O$^+$ as the proton donor. (d) Simulated current densities resulting from a microkinetic model using the DFT reaction energetics for the Cu(211) facet. A surface fraction of 5% was assumed for the 211 facet [35].

We performed constant-potential DFT[45] and microkinetic simulations for both mechanisms I and II towards CH$_4$ on four Cu facets (111, 100, 110 and 211, see also SI section 2 for computational details). As we show in section 4 of the SI, following Mechanism-I, all four facets show considerable pH dependence towards methane at high electrolyte pH, since the rate-limiting step is later than the first protonation step (N$_H$ > 1). On the 111, 110 and 211 facets, the barrier towards *CHO is lower than towards *COH. For the pathway via *CHO on the 211 facet,

14

identified as most active and shown in Figure 4(a-c), the PCET from *CHOH to *CH is limiting at low overpotentials (> 1.5V_{SHE} at pH 13) and/or high electrolyte pH (> pH 9), while the protonation of *CO to *CHO is limiting at higher overpotentials and/or low pH. The direct switch in the rate-limiting step from the first to the third elementary step arises from the facile protonation of the *CHO intermediate in the second elementary step (cf. Figure 1, C_1 pathways). We attribute the facility of this step to the configuration of *CHO, which has its O atom openly accessible to the proton donor, as well as its polarization ($\gamma_{*CHO} \approx 0.3$), as has also been observed by Liu et al.[19].

Interestingly, on the 100 facet, the barrier towards *COH is lower than that of *CHO, and at low overpotentials and/or high pH, the rate-limiting step is *COH -> *C (cf. Figure S2, S3). This is a consequence of the endergonic thermodynamics of the protonation of *CO combined with the low reverse barrier (i.e. the deprotonation of *COH) of this step. Again, in this case, at high overpotentials we find that the rate-limiting step is shifted to the first elementary step, *CO -> *COH.

Since the Cu(211) facet exhibits the highest activity in our simulations, we suggest that step sites are most likely the active sites for CH_4 production. As mentioned above, the third step in the reaction pathway is rate-limiting at low overpotentials as can be seen in the free energy diagram at ϕ_{SHE} = 3.15 eV (~-1.25 V_{SHE}) in Figure 4(a) and/or high electrolyte pH (cf. the free energy diagram at in Figure 4(b)), which leads to a simulated Tafel slope of 28 mV/dec. Figure 4(b) shows that reducing the electrolyte pH results in a change in the rate-limiting step to the first protonation step (*CO->*CHO). This change in RLS corresponds to a change of N_H from 2 to 0. As shown in Figure 2 Panel II and eq. 4, this early RLS, with N_H=0, gives rise to pH-independent activity on the SHE scale with H_2O as the proton donor, as well as, a larger Tafel slope (computed to be 96 mV/dec in our simulations). Upon reducing the pH below 4, the current at a given potential starts to increase again due to the availability of H_3O^+ as a proton donor. Interestingly, we find a negligible change in the Tafel slope upon changing the proton donor, which arises from the similarity in the symmetry factor (β) of 0.62 eV/V for the protonation of *CO by H_3O^+ (pH 3) and H_2O (pH 7 and 13).
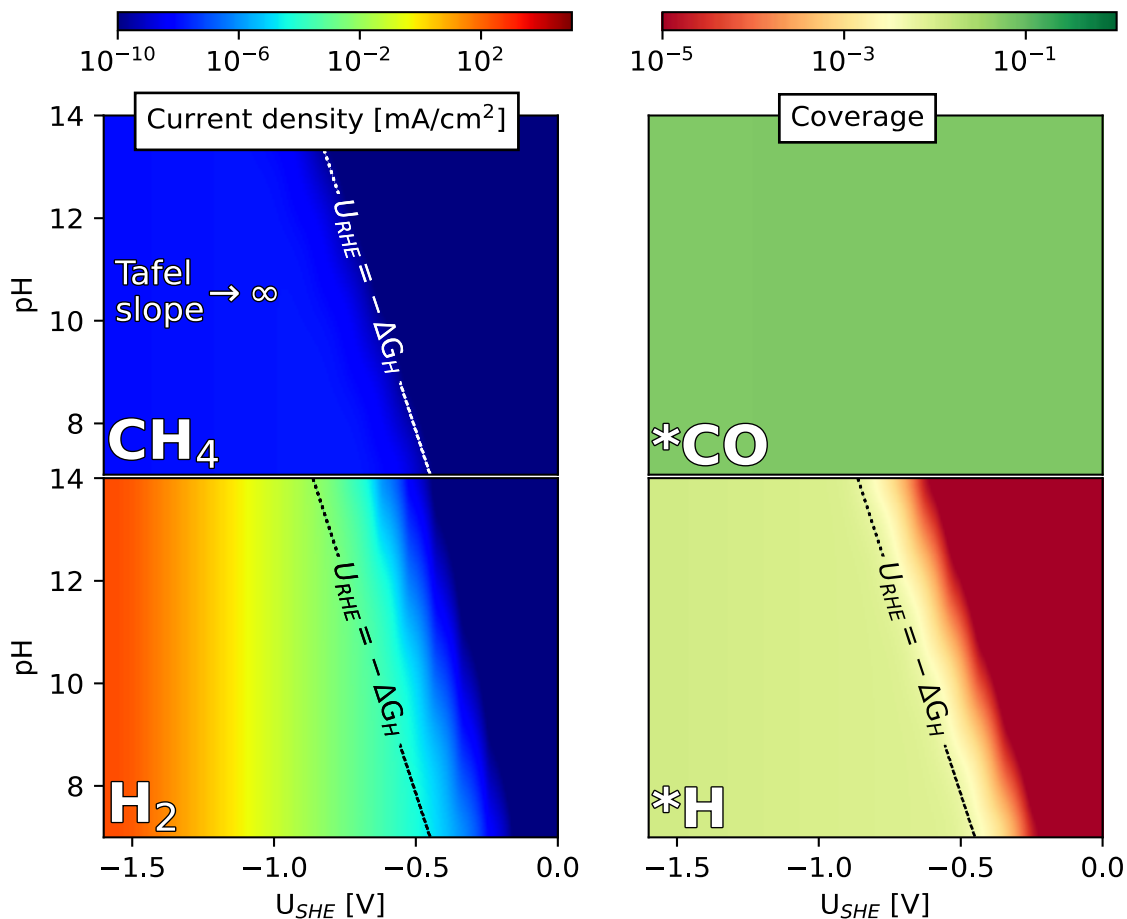
Figure 5: Simulated current densities (j) for CH$_4$ and H$_2$ (left) and coverages for *CO and *H (right) obtained from a microkinetic model for mechanism II towards CH$_4$ on Cu(211). The rate-limiting step for this pathway is the surface hydrogenation of *CO to *CHO. All the reaction energetics used in the microkinetic model have been calculated with DFT with the only exception being the reaction barrier of the hydrogen liberation (Heyrovsky) step in HER, which was adapted in order to create a non-zero hydrogen coverage. In this example, an equal symmetry factor (β = 0.36 eV/V) has been chosen for the Volmer and Heyrovsky steps, as has been calculated for the Volmer step. A detailed analysis of the effects of varying symmetry factors is provided in the section 6 of the SI.

In contrast to the observations with Mechanism-I, the simulated current densities towards CH$_4$ obtained from a microkinetic model following Mechanism-II, shown in Figure 5, lead to qualitative mismatch with the experimental results. Note that in these simulations, we chose to consider the surface hydrogenation of *CO to *CHO due to stronger binding of *CHO compared to *COH on all the investigated facets. We find this mechanism to be pH-dependent only at very low overpotentials. Additionally, the substantial potential response (i.e. low Tafel slopes) at high overpotential observed in experiments (Figure 4(a)) could not be reproduced with this model. Instead, H$_2$ production outcompetes CH$_4$ production as evident by its higher current densities. We discuss the origin of this behavior with a detailed analysis in section 6 of the SI. The major

takeaways   from   this   analysis   are   as   follows:

For Mechanism-II to reproduce the experimentally observed Tafel slopes at high pH, the hydrogen coverage needs to change exponentially with the applied potential at typical working conditions (i.e. ~ -1.4 $V_{SHE} \approx -0.7$ V_{RHE} at pH 13). The hydrogen binding free energy (ΔG_H), which varies from 0 eV to $+0.3$ eV on the investigated Cu facets, determines the ranges of potential and pH where the hydrogen coverage can change exponentially, namely at potentials (U_{RHE}) more positive than $-\Delta G_H/e$. At typical experimental conditions for COR, since the hydrogen coverage is saturated, the simulated Tafel slopes are effectively infinite (see top left panel of Figure 5).

In addition to the mismatch in the potential response with experiments, the high surface hydrogenation barrier for *CO to *CHO (~ 1 eV) computed on all the Cu facets leads to very low simulated current densities (ca. 10^{-7} mA/cm^2) even at high overpotentials. Here it is important to note that the potential response of the surface hydrogenation of *CO is nearly negligible ($\beta \approx 0$); i.e. it is a chemical process such that its activation energy is not altered by a change in U_{SHE}.

Based on above considerations and the simulated current densities based on the surface hydrogenation pathway, *we conclude that CH$_4$ production via Mechanism-II is unlikely*.

pH-dependent experiments in acidic, neutral and alkaline conditions confirm *CO dimerization and suggest a change in the RLS with pH for methane.

We validate our identified mechanisms by measuring the activity towards both C$_{2+}$ products and methane at pH 3,7 and 13. The results are shown in Figure 6, where we also included a collection of published experimental data, shown as gray bullets in the background. Our determined current densities perfectly agree with the literature data, giving us confidence in the intrinsic activity being measured. We observed a Tafel slope of well above 60 mV/dec ranging from 119 mV/dec at pH 13 to 199mV/dec at pH 7 and in all cases little pH dependence even in acidic conditions (pH 3), where either the buffering anion species [65–67] or H$_3$O$^+$ might be viable proton donors. This confirms that CO coupling is the RLS towards C$_{2+}$ products. If a PCET step would be rate-limiting at pH 3, it would show an increase in the measured C$_{2+}$ activity vs. the situation where H$_2$O is the proton donor (cf. Figure 2, panel II, right). In contrast, we see that the measured current density towards C$_{2+}$ products at pH 3 shows a slight decrease compared to neutral/alkaline electrolytes which may originate from specific adsorption of buffering anions[65] thereby blocking active sites and/or competition from CH$_4$ production, which depletes *CO. Therefore, we conclude that a proton transfer is not involved in the RLS towards C$_{2+}$ products, which points to CO-CO dimerization as the rate limiting step at all investigated pH values (3-13) and is consistent with our simulations.

We note that with mass-transport limitations associated with the diffusion of protons/buffer species, it is possible that even under acidic conditions (pH 3), H$_2$O is the only viable proton donor (at pH 3, $c_{H+,bulk} = 10^{-3}$ M while $c_{water} = 55$ M) such that PCET from H$_2$O to the *OCCO dimer intermediate can be the rate-limiting step. This scenario would also give rise to a high Tafel slope (> 60 mV/dec) and no effect of pH on activity amongst the measurements at different pH (cf Figure 2, panel II, left). However, both the measured current densities towards CH$_4$ (see Figure 6b) and H$_2$ (see SI section 7) for pH 3, 7 and 13 suggest a proton donor other than H$_2$O at pH 3: as expected from Fig. 2 for the case where H$_3$O$^+$ is the proton donor, the PCET limited current densities decrease with an increase in the electrolyte pH. This observation implies that sufficient concentration of proton donors other than H$_2$O (i.e. H$_3$O$^+$ and/or buffer species) are available at pH 3.

Our conclusion of *CO dimerization being rate limiting is reflected in the data collection taken from literature given as grey bullets in Figure 6(a) and shown in more detail in section 10 of the SI. In this data collection, we include experimental data from both CO_2 and CO reduction on Cu electrodes varying the pH from 7 to 14. The overlap of both CO and CO_2 reduction data suggests that *CO is a crucial intermediate, whose coverage is independent of whether it is created in the reduction process (CO2R) or directly fed in (COR). This strongly suggests that its coverage is saturated and determined by equilibration with gas phase CO. Our simulations show the same trends: In Figure S4 we show the simulated *CO coverages. On all simulated facets the coverage is below 40%, as a consequence of the steep rise in *CO-*CO interactions at elevated coverages. Additionally, the small surface dipole created during the adsorption of *CO, leads to a negligible potential response of its coverage (see also SI section 12 for the tabulated potential responses), with the exception of the 110 facet which shows a steep reduction in *CO coverage at higher overpotential, due to the build-up of a *CHO coverage.
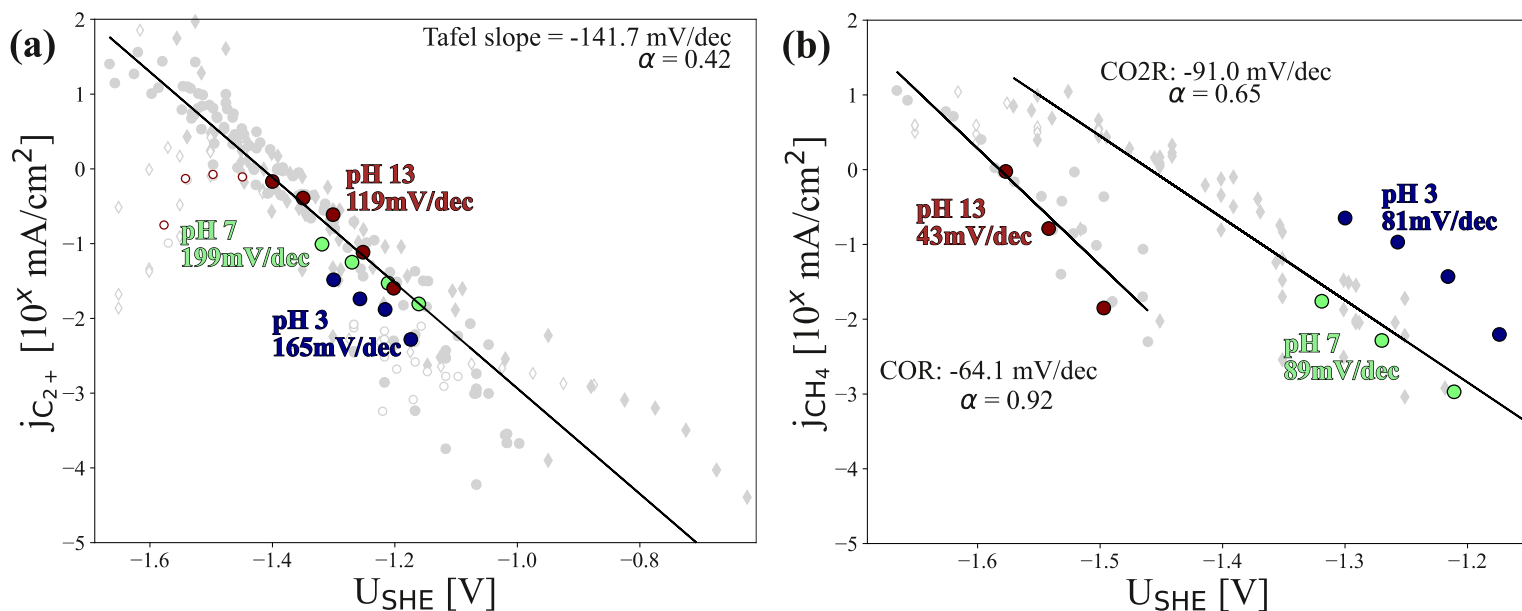

Figure 6: Measured current densities at pH 3, 7 and 13 for towards both (a) C_{2+} products and (b) methane on polycrystalline Cu foil. Additionally, a Tafel analysis based on a collection of experimental studies including both CO and CO_2 reduction experiments are included as grey markers for benchmarking. All included current densities have been normalized with respect to the electrochemically active surface area (ECSA). Open markers represent measurements that are likely convoluted with mass transport and therefore have not been included in the estimation of the Tafel slopes. The partial current densities resulting from CO_2 reduction (pH~7) and CO reduction (pH~13) are marked as diamonds and circles, respectively. The individual Tafel slopes and respective references are given in the SI section 9.

A fit over all the data also gives an overall Tafel slope of ~ 140 mV/dec in reasonable agreement with the measured values reported of our study, being 171mV/dec from theory and 119-199mV/dec from measurements. This result further strengthens the analysis shown in Figure 3 and its conclusion that the coupling of 2 *CO molecules to form the *OCCO dimer species is the rate-

18

limiting step for $CO_{(2)}R$ towards C_{2+} products. Interestingly, although a wide range of nanostructured Cu surfaces and experimental setups including H-cells and gas diffusion electrodes (GDEs) are compared in the plot, the spread of the current density seems to be within an order of magnitude, as noted in previous studies [3,68]. This spread suggests that the number of active sites differs by less than a factor of 5. We postulate that the restructuring of copper at reaction conditions might be at play here, as the surface has been shown to be dynamic in electrochemical $CO_{(2)}R$ experiments [69].

Figure 6b shows the measured partial current densities towards methane at pH 3, 7 and 13, which in contrast to C_{2+} products, exhibit pH dependent activity and smaller Tafel slopes (43-89 mV/dec) with increasing pH, and a decrease in these Tafel slopes with respect to U_{SHE}. These different features indicate that the mechanism for methane production differs fundamentally from the C_{2+} pathway. We find a Tafel slope of 43 mV/dec at pH 13, which suggests that the second PCET step is rate limiting ($N_H > 0$, cf. Eq. 3 and the scheme shown in Figure 2 (II). Such a low Tafel slope also indicates that a step beyond the first PCET is rate limiting as was already put forth by Hori et al [8,9]. We note that if CO transport limitations are present at such negative potentials, the corresponding intrinsic Tafel slope would be even smaller, which would still imply that a later step is rate limiting. At lower pH values of 3 and 7, the Tafel slope is above 80 mV/dec, which suggests that the RLS is the first PCET step ($N_H = 0$). The measured current densities do not overlap for these two pH values on the SHE scale, which indicates that the proton donor is different in the two measurements. At pH 7, only water and buffer species are viable proton donors, while at pH 3, H_3O^+ species might also be a viable proton donor.

In contrast to the Tafel analysis for C_{2+} products, by analyzing recently published results for methane production, shown as gray markers in Figure 6b, we could clearly identify two distinct regions. These two regions, in contrast to Hori's data [8,9], are visible even if the current density is "corrected" by the electrolyte pH (see SI section 11). The first region corresponds to measurements performed with CO_2 as the reactant at pH close to 7 with a Tafel slope of above 60 mV dec^{-1}, the second is a result of studies starting from CO, performed at higher pH values (pH $\sim$ 13) exhibiting an overall Tafel slope of $\sim$60mV/dec. We note that the smaller number of data points and high degree of noise at high pH precludes as reliable a mechanistic interpretation. However, we do observe a reduction in both the mean (cf. Figure 6) and especially the individual Tafel slopes (cf. Figure S16) and the partial current density towards CH_4 for experiments performed in alkaline conditions (pH $\sim$ 13) suggesting a rate-limiting step beyond the first PCET step, in agreement with the findings of the present study.

Discussion of discrepancies between theory and experiment

While our simulations show qualitative agreement with experiments at reducing potentials negative of -1.4 V_{SHE}, it is important to note that quantitative differences between experimental and theoretical kinetics at lower overpotentials can arise from several sources. Typical DFT errors for surface reaction energetics are 0.15 eV [60], but in computational electrochemistry this uncertainty is compounded by several other contributions. Firstly, we convert the workfunction (ϕ) from our ab initio constant potential simulations to a potential vs. the SHE scale (V_{SHE}) using work function for SHE determined by Trassati from experiments ($\phi_{SHE} = 4.4 \ eV$)[62], and not an internal, computed ϕ_{SHE} reference from our model. Additionally, the computational model used in this work for calculating the reaction energetics is a simplified model of the electrode-electrolyte interface. First, the static water layer that was used in our simulations might substantially reduce the degrees of freedom of H_2O molecules, and does not correspond to the (dynamic) electrode-

electrolyte interface present under experimental conditions[70]. Second, no explicit ions have been used in the determination of the reaction barriers, hence we do not include any local interactions between ions and transition states that could potentially be present at the electrode-electrolyte interface. [71] Finally, the calculation of electrochemical barriers on the basis of grand-canonical DFT with a combination of implicit and explicit solvation is still a fairly new concept and further improvements and shortcomings of these methods have already been pointed out in previous work[72–74].

From an experimental standpoint, several factors might convolute analysis of the intrinsic reaction kinetics, including mass transport limitations of the reactant species (e.g., CO and the proton donors), the detection sensitivities for product analysis, and deactivation/dynamic changes of the surface active-sites. We observed a small diffusion-limited CO reduction partial current density (< 1 mA cm^{-2}) due to the extremely low solubility of CO in aqueous electrolyte (~ 1 mM under our testing conditions[75]) and the relatively thick boundary layer (~ 80 μm[76]) of our electrochemical cell. In addition, the partial current densities (or activity) of CO reduction are obtained based on *ex situ* analytical methods (i.e., GC and NMR), that provide averaged values from electrolysis time scales of tens of minutes. Therefore, these data cannot fully represent the true kinetics at the electrode/electrolyte interface unless the system is continuously under steady-state conditions, which is rarely the case. In fact, Cu-based electrodes can undergo dynamic changes in morphology[22,77], surface faceting[78] and oxidation states[79] that affect the reaction kinetics. Thus, we suggest the development of new product analysis strategies that enable the collection of more accurate kinetic data with improved temporal resolution will strengthen correlations between experiment and theory[80–82].

Implications for future mechanistic studies and catalyst design

Although the present mechanistic studies show *CO dimerization to be the rate limiting step for C$_{2+}$ products on Cu electrodes is conclusive, alternative experiments investigating the involvement of a proton in the rate-limiting step could still be performed. The substitution of H$_2$O with D$_2$O might lead to a measurable KIE effect for a rate-limiting step involving a proton transfer, while having little/no effect for a potential-dependent chemical rate-limiting step (i.e. *CO dimerization). However, we note that the effect might be too small for definite exclusion of one or the other mechanism[29]. Resasco *et al.* [66] recently showed that the current densities measured in strongly buffered electrolytes linearly depends on the concentration of the buffering anion. Hence, further studies on the influence of electrolyte buffers on the performance in CO$_{(2)}$R can also provide important insights into the distinction in the nature of the rate-limiting step. Finally, experiments performed at lower overpotentials than those that have been investigated in this work might be able to observe a change in the rate-limiting step from *OCCO protonation to *CO dimerization that was predicted by our *ab-initio* kinetics simulations. We note that such a study might necessitate surfaces with high roughness factors such as oxide derived Cu (OD-Cu), [83] and/or setups with high product sensitivity in order to obtain measurable current densities at low overpotentials.

For theoretical studies, we emphasize that it is crucial to incorporate the effect of potential sensitivity due to charge reorganization (denoted in this work as γ) in simulations of multi-step electrochemical reactions. This is exemplified by the rate limiting CO dimerization step for the production of multicarbon products that exhibits a significant potential response. Additionally, we emphasize that accounting for the whole reaction process up to the rate limiting step, with the inclusion of reaction kinetics, is crucial for a benchmark of the calculated results to experimental

observables, since pH and potential dependence cannot be estimated from single elementary steps. Finally, a thorough understanding of electrochemical reactions at the solid/liquid interface, in principle, would also benefit from multiscale models that account for mass transport including diffusion and migration of species.

From an experimental standpoint, we emphasize the need to develop new reactor-designs and product analyzing techniques that can enable the collection of more precise and time-resolved intrinsic kinetic data in an extended electrode potential window. More robust kinetic information can be better interpreted by theoretical models, thereby providing new insights to guide the design of more active and selective catalysts.

Based on the identified rate-determining steps for the production of methane and C_{2+} products, we are also in a position to suggest general principles for future catalyst design. Since the formation of multicarbon products is limited by *CO dimerization, the binding energy of *OCCO can serve as an important descriptor for the identification of electrode materials with high activity towards multicarbon products. Furthermore, since no proton is involved in the RLS, working in buffer free electrolytes or using buffers unable to act as proton donors (i.e. "innocent" buffers) is recommended for high C_{2+} yield[46,66]. Finally, the use of Cs^+ over other alkali-metal cations has been shown to improve $eCO_{(2)}R$ activity towards multicarbon products.[84] We attribute this behavior to the substantial dipole moment of *OCCO, similar to previous results for CO_2 reduction to CO.[29]

For methane, as we find the rate-limiting step to involve a proton transfer step, buffering anions with a lower pK_a than water can be used as proton donors (i.e. "non-innocent" buffers) to accelerate the rate limiting step for methane production.[66] Additionally, since we conclusively exclude surface hydrogenation as the rate-limiting step for methane production, the negative order in CO reported in previous studies that has been attributed to involvement of the surface hydrogenation involving *CO and *H would also need to be reconsidered.[31,43]

CONCLUSIONS

Elucidating the reaction pathways including the rate-limiting steps in electrochemical $CO_{(2)}$ reduction (eCO_2R) is challenging due to the complexity of the reaction mechanisms towards C_1 and C_{2+} products. Based on pH resolved experiments reaching down to acidic conditions, necessary to unequivocally exclude the involvement of a proton transfer in the rate-limiting step, and constant potential *ab-initio* calculations including both H_2O and H_3O^+ proton donors, we demonstrated that only a reaction whose rate is limited by the coupling of two CO molecules is able to explain the measured results for $eCO_{(2)}R$ to multicarbon products. Two independent approaches in the analysis resulted in the same result, namely the absence of a change in current density upon change in proton donor and the lower potential response to current density as compared to the protonation of *OCCO. Our analysis suggests a transition in the RLS from *CO dimerization to *OCCO protonation might be possible at low overpotentials that has not been so far observed within the potential ranges probed in the experiments.

For methane formation, we conclusively excluded a mechanism based on the surface combination of *CO and *H, since it would lead to both undetectable current densities and close to infinite Tafel slopes at reaction conditions. On the other hand, a fully electrochemical mechanism explains the experimentally observed activities. We identified a change in the rate limiting step with the electrolyte pH for methane production. While at neutral and acidic conditions

the first PCET step is rate limiting, at pH > 9, the third step is rate limiting, leading to a pH dependence of the mechanism only in alkaline conditions.

Overall our analysis conclusively elucidates the rate limiting steps in eCO$_{(2)}$R towards both methane and C$_{2+}$ products. The results also suggest that electrocatalysts which stabilize the *OCCO dimer beyond Cu to be alternative candidates for the production of high value C$_2$ products.

ASSOCIATED CONTENT

Supporting Information

Experimental methods, Computational details, Energetics towards C$_{2+}$ products via *CO dimerization on varying facets, Energetics towards CH$_4$ on varying facets, Simulated *CO coverage at varying potential and pH, Considerations on methane production being limited by a chemical step, Measured current densities of hydrogen evolution reaction (HER), Qualitative scheme for estimating the potential and pH dependence of electrochemical reactions, pH dependence and energetics on the RHE scale, Individual Tafel slopes of measurements in experimental database, pH corrected experimental database for CH$_4$ and tabulated DFT based energetics.

All the data needed to reproduce the results as well as analysis routines are publicly available and can be downloaded from the gitlab repository: https://gitlab.com/gkastlun/ph-in-cor.

AUTHOR INFORMATION

Corresponding Author
*Georg Kastlunger (geokast@dtu.dk)

Author Contributions
GK, HHH, SR and KC conceived the idea of the work; GK and HHH performed the calculations; LW performed the experiments; GK, HHH, NG and KC wrote the article; All authors edited the manuscript. KC, TJ, and CH supervised the work and the writing of the article.

REFERENCES

(1)   Bushuyev, O. S.; De Luna, P.; Dinh, C. T.; Tao, L.; Saur, G.; van de Lagemaat, J.; Kelley, S. O.; Sargent, E. H. What Should We Make with CO2 and How Can We Make It? *Joule* **2018**, *2* (5), 825–832. https://doi.org/10.1016/j.joule.2017.09.003.

(2)   De Luna, P.; Hahn, C.; Higgins, D.; Jaffer, S. A.; Jaramillo, T. F.; Sargent, E. H. What Would It Take for Renewably Powered Electrosynthesis to Displace Petrochemical Processes? *Science (80-.).* **2019**, *364* (6438), eaav3506. https://doi.org/10.1126/science.aav3506.

(3)   Nitopi, S.; Bertheussen, E.; Scott, S. B.; Liu, X.; Engstfeld, A. K.; Horch, S.; Seger, B.; Stephens, I. E. L.; Chan, K.; Hahn, C.; Nørskov, J. K.; Jaramillo, T. F.; Chorkendorff, I. Progress and Perspectives of Electrochemical CO 2 Reduction on Copper in Aqueous Electrolyte. *Chem. Rev.* **2019**, *119* (12), 7610–7672. https://doi.org/10.1021/acs.chemrev.8b00705.

(4)   Karimi, M.; Hillestad, M.; Svendsen, H. F. Capital Costs and Energy Considerations of Different Alternative Stripper Configurations for Post Combustion CO2 Capture. *Chem. Eng. Res. Des.* **2011**, *89* (8), 1229–1236. https://doi.org/10.1016/j.cherd.2011.03.005.

(5)   Øi, L. E.; Kvam, S. H. P. Comparison of Energy Consumption for Different CO2 Absorption Configurations Using Different Simulation Tools. *Energy Procedia* **2014**, *63*, 1186–1195. https://doi.org/10.1016/j.egypro.2014.11.128.

(6)   Kiani, A.; Jiang, K.; Feron, P. Techno-Economic Assessment for CO2 Capture From Air Using a Conventional Liquid-Based Absorption Process. *Front. Energy Res.* **2020**, *8*, 92. https://doi.org/10.3389/fenrg.2020.00092.

(7)   Greenblatt, J. B.; Miller, D. J.; Ager, J. W.; Houle, F. A.; Sharp, I. D. The Technical and Energetic Challenges of Separating (Photo)Electrochemical Carbon Dioxide Reduction Products. *Joule* **2018**, *2* (3), 381–420. https://doi.org/10.1016/j.joule.2018.01.014.

(8)   Hori, Y.; Takahashi, R.; Yoshinami, Y.; Murata, A. Electrochemical Reduction of CO at a Copper Electrode. *J. Phys. Chem. B* **1997**, *101*, 7075–7081.

(9)   Hori, Y. Electrochemical CO2 Reduction on Metal Electrodes. In *Modern Aspects of Electrochemistry*; Springer New York: New York, NY, 2008; pp 89–189. https://doi.org/10.1007/978-0-387-49489-0_3.

(10)   Schouten, K. J. P.; Kwon, Y.; van der Ham, C. J. M.; Qin, Z.; Koper, M. T. M. A New Mechanism for the Selectivity to C1 and C2 Species in the Electrochemical Reduction of Carbon Dioxide on Copper Electrodes. *Chem. Sci.* **2011**, *2* (10), 1902. https://doi.org/10.1039/c1sc00277e.

(11)   Schouten, K. J. P.; Qin, Z.; Gallent, E. P.; Koper, M. T. M. Two Pathways for the Formation of Ethylene in CO Reduction on Single-Crystal Copper Electrodes. *J. Am. Chem. Soc.* **2012**, *134* (24), 9864–9867. https://doi.org/10.1021/ja302668n.

(12)   Calle-Vallejo, F.; Koper, M. T. M. Theoretical Considerations on the Electroreduction of CO to C 2 Species on Cu(100) Electrodes. *Angew. Chemie Int. Ed.* **2013**, *52* (28), 7282–7285. https://doi.org/10.1002/anie.201301470.

(13)   Nie, X.; Luo, W.; Janik, M. J.; Asthagiri, A. Reaction Mechanisms of CO2 Electrochemical Reduction on Cu(111) Determined with Density Functional Theory. *J. Catal.* **2014**, *312*, 108–122. https://doi.org/10.1016/j.jcat.2014.01.013.

(14)   Luo, W.; Nie, X.; Janik, M. J.; Asthagiri, A. Facet Dependence of CO 2 Reduction Paths on Cu Electrodes. *ACS Catal.* **2016**, *6* (1), 219–229. https://doi.org/10.1021/acscatal.5b01967.

(15)   Göttle, A. J.; Koper, M. T. M. Proton-Coupled Electron Transfer in the Electrocatalysis of CO 2 Reduction: Prediction of Sequential vs. Concerted Pathways Using DFT. *Chem. Sci.* **2017**, *8* (1), 458–465. https://doi.org/10.1039/C6SC02984A.

(16)   Garza, A. J.; Bell, A. T.; Head-Gordon, M. Mechanism of CO2 Reduction at Copper Surfaces: Pathways to C2 Products. *ACS Catal.* **2018**, *8* (2), 1490–1499. https://doi.org/10.1021/acscatal.7b03477.

(17)   Bagger, A.; Ju, W.; Varela, A. S.; Strasser, P.; Rossmeisl, J. Electrochemical CO 2 Reduction: Classifying Cu Facets. *ACS Catal.* **2019**, *9* (9), 7894–7899. https://doi.org/10.1021/acscatal.9b01899.

(18)   Mangione, G.; Huang, J.; Buonsanti, R.; Corminboeuf, C. C. Dual-Facet Mechanism in Copper Nanocubes for Electrochemical CO 2 Reduction into Ethylene. *J. Phys. Chem. Lett* **2019**, *10*, 4265. https://doi.org/10.1021/acs.jpclett.9b01471.

(19)   Liu, X.; Schlexer, P.; Xiao, J.; Ji, Y.; Wang, L.; Sandberg, R. B.; Tang, M.; Brown, K. S.; Peng, H.; Ringe, S.; Hahn, C.; Jaramillo, T. F.; Nørskov, J. K.; Chan, K. PH Effects on the Electrochemical Reduction of CO (2) towards C 2 Products on Stepped Copper. *Nat. Commun.* **2019**, *10* (1), 1–10. https://doi.org/10.1038/s41467-018-07970-9.

(20)   Schouten, K. J. P.; Qin, Z.; Gallent, E. P.; Koper, M. T. M. Two Pathways for the Formation of Ethylene in CO Reduction on Single-Crystal Copper Electrodes. *J. Am. Chem. Soc.* **2012**, *134* (24), 9864–9867. https://doi.org/10.1021/ja302668n.

(21)   Zhuang, T.-T.; Liang, Z.-Q.; Seifitokaldani, A.; Li, Y.; De Luna, P.; Burdyny, T.; Che, F.; Meng, F.; Min, Y.; Quintero-Bermudez, R.; Dinh, C. T.; Pang, Y.; Zhong, M.; Zhang, B.; Li, J.; Chen, P.-N.; Zheng, X.-L.; Liang, H.; Ge, W.-N.; Ye, B.-J.; Sinton, D.; Yu, S.-H.; Sargent, E. H. Steering Post-C–C Coupling Selectivity Enables High Efficiency Electroreduction of Carbon Dioxide to Multi-Carbon Alcohols. *Nat. Catal.* **2018**, *1* (6), 421–428. https://doi.org/10.1038/s41929-018-0084-7.

(22)   Wang, X.; de Araújo, J. F.; Ju, W.; Bagger, A.; Schmies, H.; Kühl, S.; Rossmeisl, J.; Strasser, P. Mechanistic Reaction Pathways of Enhanced Ethylene Yields during Electroreduction of CO2–CO Co-Feeds on Cu and Cu-Tandem Electrocatalysts. *Nat. Nanotechnol.* **2019**, *14* (11), 1063–1070. https://doi.org/10.1038/s41565-019-0551-6.

(23)   Birdja, Y. Y.; Pérez-Gallent, E.; Figueiredo, M. C.; Göttle, A. J.; Calle-Vallejo, F.; Koper, M. T. M. Advances and Challenges in Understanding the Electrocatalytic Conversion of Carbon Dioxide to Fuels. *Nat. Energy* **2019**, *4* (9), 732–745. https://doi.org/10.1038/s41560-019-0450-y.

(24)   Garza, A. J.; Bell, A. T.; Head-Gordon, M. Mechanism of CO 2 Reduction at Copper Surfaces: Pathways to C 2 Products. *ACS Catal.* **2018**, *8* (2), 1490–1499. https://doi.org/10.1021/acscatal.7b03477.

(25)   Mangione, G.; Huang, J.; Buonsanti, R.; Corminboeuf, C. C. Dual-Facet Mechanism in Copper Nanocubes for Electrochemical CO 2 Reduction into Ethylene. *J. Phys. Chem. Lett* **2019**, *10*, 4265. https://doi.org/10.1021/acs.jpclett.9b01471.

(26)   Iyengar, P.; Kolb, M. J.; Pankhurst, J. R.; Calle-Vallejo, F.; Buonsanti, R. Elucidating the Facet-Dependent Selectivity for CO 2 Electroreduction to Ethanol of Cu–Ag Tandem Catalysts. *ACS Catal.* **2021**, *11* (8), 4456–4463. https://doi.org/10.1021/acscatal.1c00420.

(27)   Kim, J. Y.; Park, W.; Choi, C.; Kim, G.; Cho, K. M.; Lim, J.; Kim, S. J.; Al-Saggaf, A.; Gereige, I.; Lee, H.; Jung, W.-B.; Jung, Y.; Jung, H.-T. High Facets on Nanowrinkled Cu via Chemical Vapor Deposition Graphene Growth for Efficient CO 2 Reduction into Ethanol. *ACS Catal.* **2021**, *11*, 5658–5665. https://doi.org/10.1021/acscatal.0c05263.

(28)   Peng, H.; Tang, M. T.; Liu, X.; Schlexer Lamoureux, P.; Bajdich, M.; Abild-Pedersen, F. The Role of Atomic Carbon in Directing Electrochemical CO (2) Reduction to Multicarbon Products. *Energy Environ. Sci.* **2021**, *14* (1), 473–482. https://doi.org/10.1039/D0EE02826F.

(29)   Ringe, S.; Morales-Guio, C. G.; Chen, L. D.; Fields, M.; Jaramillo, T. F.; Hahn, C.; Chan, K. Double Layer Charging Driven Carbon Dioxide Adsorption Limits the Rate of Electrochemical Carbon Dioxide Reduction on Gold. *Nat. Commun.* **2020**, *11* (1), 33. https://doi.org/10.1038/s41467-019-13777-z.

(30)   Wang, L.; Nitopi, S. A.; Bertheussen, E.; Orazov, M.; Morales-Guio, C. G.; Liu, X.; Higgins, D. C.; Chan, K.; Nørskov, J. K.; Hahn, C.; Jaramillo, T. F. Electrochemical Carbon Monoxide Reduction on Polycrystalline Copper: Effects of Potential, Pressure, and PH on Selectivity toward Multicarbon and Oxygenated Products. *ACS Catal.* **2018**, *8* (8), 7445–7454. https://doi.org/10.1021/acscatal.8b01200.

(31)   Li, J.; Chang, X.; Zhang, H.; Malkani, A. S.; Cheng, M.; Xu, B.; Lu, Q. Electrokinetic and in Situ Spectroscopic Investigations of CO Electrochemical Reduction on Copper. *Nat. Commun.* **2021**, *12* (1), 3264. https://doi.org/10.1038/s41467-021-23582-2.

(32)   Peterson, A. A.; Abild-Pedersen, F.; Studt, F.; Rossmeisl, J.; Nørskov, J. K. How Copper Catalyzes the Electroreduction of Carbon Dioxide into Hydrocarbon Fuels. *Energy Environ. Sci.* **2010**, *3* (9), 1311. https://doi.org/10.1039/c0ee00071j.

(33)   Nie, X.; Luo, W.; Janik, M. J.; Asthagiri, A. Reaction Mechanisms of CO2 Electrochemical Reduction on Cu(111) Determined with Density Functional Theory. *J. Catal.* **2014**, *312*, 108–122. https://doi.org/10.1016/j.jcat.2014.01.013.

(34)   Goodpaster, J. D.; Bell, A. T.; Head-Gordon, M. Identification of Possible Pathways for C–C Bond Formation during Electrochemical Reduction of CO 2 : New Theoretical Insights from an Improved Electrochemical Model. *J. Phys. Chem. Lett.* **2016**, *7* (8), 1471–1477. https://doi.org/10.1021/acs.jpclett.6b00358.

(35)   Liu, X.; Xiao, J.; Peng, H.; Hong, X.; Chan, K.; Nørskov, J. K. Understanding Trends in Electrochemical Carbon Dioxide Reduction Rates. *Nat. Commun.* **2017**, *8* (1), 15438. https://doi.org/10.1038/ncomms15438.

(36)   Xiao, H.; Cheng, T.; Goddard, W. A. Atomistic Mechanisms Underlying Selectivities in C 1 and C 2 Products from Electrochemical Reduction of CO on Cu(111). *J. Am. Chem. Soc.* **2017**, *139* (1), 130–136. https://doi.org/10.1021/jacs.6b06846.

(37)   Gattrell, M.; Gupta, N.; Co, A. A Review of the Aqueous Electrochemical Reduction of CO2 to Hydrocarbons at Copper. *J. Electroanal. Chem.* **2006**, *594* (1), 1–19. https://doi.org/10.1016/j.jelechem.2006.05.013.

(38)   Tang, W.; Peterson, A. A.; Varela, A. S.; Jovanov, Z. P.; Bech, L.; Durand, W. J.; Dahl, S.; Nørskov, J. K.; Chorkendorff, I. The Importance of Surface Morphology in Controlling the Selectivity of Polycrystalline Copper for CO 2 Electroreductionw. *Phys. Chem. Chem. Phys* **2012**, *14*, 76–81. https://doi.org/10.1039/c1cp22700a.

(39)   Laborda, E.; Henstridge, M. C.; Compton, R. G. Giving Physical Insight into the Butler–Volmer Model of Electrode Kinetics: Part 2 – Nonlinear Solvation Effects on the Voltammetry of Heterogeneous Electron Transfer Processes. *J. Electroanal. Chem.* **2012**, *681*, 96–102. https://doi.org/10.1016/J.JELECHEM.2012.06.008.

(40)   Luo, W.; Xie, W.; Mutschler, R.; Oveisi, E.; De Gregorio, G. L.; Buonsanti, R.; Züttel, A. Selective and Stable Electroreduction of CO 2 to CO at the Copper/Indium Interface. *ACS Catal.* **2018**, *8* (7), 6571–6581. https://doi.org/10.1021/acscatal.7b04457.

(41)   Luc, W.; Fu, X.; Shi, J.; Lv, J.-J.; Jouny, M.; Ko, B. H.; Xu, Y.; Tu, Q.; Hu, X.; Wu, J.; Yue, Q.; Liu, Y.; Jiao, F.; Kang, Y. Two-Dimensional Copper Nanosheets for Electrochemical Reduction of Carbon Monoxide to Acetate. *Nat. Catal.* **2019**, *2* (5), 423–430. https://doi.org/10.1038/s41929-019-0269-8.

(42)   Ripatti, D. S.; Veltman, T. R.; Kanan, M. W. Carbon Monoxide Gas Diffusion Electrolysis That Produces Concentrated C2 Products with High Single-Pass Conversion. *Joule* **2019**, *3* (10), 2581. https://doi.org/10.1016/j.joule.2019.09.012.

(43)   Schreier, M.; Yoon, Y.; Jackson, M. N.; Surendranath, Y. Competition between H and CO for Active Sites Governs Copper-Mediated Electrosynthesis of Hydrocarbon Fuels. *Angew. Chemie Int. Ed.* **2018**, *57* (32), 10221–10225. https://doi.org/10.1002/anie.201806051.

(44)   Li, J.; Chang, K.; Zhang, H.; He, M.; Goddard, W. A.; Chen, J. G.; Cheng, M. J.; Lu, Q. Effectively Increased Efficiency for Electroreduction of Carbon Monoxide Using Supported Polycrystalline Copper Powder Electrocatalysts. *ACS Catal.* **2019**, *9* (6), 4709–4718. https://doi.org/10.1021/acscatal.9b00099.

(45)   Kastlunger, G.; Lindgren, P.; Peterson, A. A. Controlled-Potential Simulation of Elementary Electrochemical Reactions: Proton Discharge on Metal Surfaces. *J. Phys. Chem. C* **2018**, *122* (24), 12771–12781. https://doi.org/10.1021/acs.jpcc.8b02465.

(46)   Jackson, M. N.; Jung, O.; Lamotte, H. C.; Surendranath, Y. Donor-Dependent Promotion of Interfacial Proton-Coupled Electron Transfer in Aqueous Electrocatalysis. *ACS Catal* **2019**, *9*, 2021. https://doi.org/10.1021/acscatal.9b00056.

(47)   Nørskov, J. K.; Rossmeisl, J.; Logadottir, A.; Lindqvist, L.; Kitchin, J. R.; Bligaard, T.; Jónsson, H. Origin of the Overpotential for Oxygen Reduction at a Fuel-Cell Cathode. *J. Phys. Chem. B* **2004**, *108* (46), 17886–17892. https://doi.org/10.1021/jp047349j.

(48)   Vijay, S.; Ju, W.; Brückner, S.; Tsang, S.-C.; Strasser, P.; Chan, K. Unified Mechanistic Understanding of CO2 Reduction to CO on Transition Metal and Single Atom Catalysts. *Nat. Catal.* **2021**, 1–8. https://doi.org/10.1038/s41929-021-00705-y.

(49)   Guidelli, R.; Compton, R. G.; Feliu, J. M.; Gileadi, E.; Lipkowski, J.; Schmickler, W.; Trasatti, S. Definition of the Transfer Coefficient in Electrochemistry (IUPAC Recommendations 2014). *Pure Appl. Chem.* **2014**, *86* (2), 259–262. https://doi.org/10.1515/pac-2014-5025.

(50)   Lindgren, P.; Kastlunger, G.; Peterson, A. A. A Challenge to the G ∼ 0 Interpretation of Hydrogen Evolution. *ACS Catal.* **2019**, *10* (1), 121–128. https://doi.org/10.1021/ACSCATAL.9B02799.

(51)   Limaye, A. M.; Zeng, J. S.; Willard, A. P.; Manthiram, K. Bayesian Data Analysis Reveals No Preference for Cardinal Tafel Slopes in CO2 Reduction Electrocatalysis. *Nat. Commun.* **2021**, *12* (1), 703. https://doi.org/10.1038/s41467-021-20924-y.

(52)   Kastlunger, G.; Lindgren, P.; Peterson, A. A. Controlled-Potential Simulation of Elementary Electrochemical Reactions : Proton Discharge on Metal Surfaces. *J. Phys. Chem. C* **2018**, *122*, 12771–12781. https://doi.org/10.1021/acs.jpcc.8b02465.

(53)   Li, H.; Li, Y.; Koper, M. T. M.; Calle-Vallejo, F. Bond-Making and Breaking between Carbon, Nitrogen, and Oxygen in Electrocatalysis. *J. Am. Chem. Soc.* **2014**, *136* (44), 15694–15701. https://doi.org/10.1021/ja508649p.

(54)   Wang, Y.; Shen, H.; Livi, K. J. T.; Raciti, D.; Zong, H.; Gregg, J.; Onadeko, M.; Wan, Y.; Watson, A.; Wang, C. Copper Nanocubes for CO 2 Reduction in Gas Diffusion Electrodes. *Nano Lett.* **2019**, *19* (12), 8461–8468. https://doi.org/10.1021/acs.nanolett.9b02748.

(55)   Jiang, K.; Sandberg, R. B.; Akey, A. J.; Liu, X.; Bell, D. C.; Nørskov, J. K.; Chan, K.; Wang, H. Metal Ion Cycling of Cu Foil for Selective C–C Coupling in Electrochemical CO2 Reduction. *Nat. Catal.* **2018**, *1* (2), 111–119. https://doi.org/10.1038/s41929-017-0009-x.

(56)   Huang, Y.; Handoko, A. D.; Hirunsit, P.; Yeo, B. S. Electrochemical Reduction of CO 2 Using Copper Single-Crystal Surfaces: Effects of CO* Coverage on the Selective Formation of Ethylene. *ACS Catal.* **2017**, *7* (3), 1749–1756. https://doi.org/10.1021/acscatal.6b03147.

(57)   Zhdanov, V. P.; Kasemo, B. *Kinetics of Rapid Heterogeneous Reactions on the Nanometer Scale*; 1997; Vol. 170.

(58)   Nørskov, J. K.; Bligaard, T.; Hvolbæk, B.; Abild-Pedersen, F.; Chorkendorff, I.; Christensen, C. H. The Nature of the Active Site in Heterogeneous Metal Catalysis. *Chem. Soc. Rev.* **2008**, *37* (10), 2163. https://doi.org/10.1039/b800260f.

(59)   Tran, R.; Xu, Z.; Radhakrishnan, B.; Winston, D.; Sun, W.; Persson, K. A.; Ong, S. P. Surface Energies of Elemental Crystals. *Sci. Data* **2016**, *3* (1), 160080. https://doi.org/10.1038/sdata.2016.80.

(60)   Medford, A. J.; Wellendorff, J.; Vojvodic, A.; Studt, F.; Abild-Pedersen, F.; Jacobsen, K. W.; Bligaard, T.; Nørskov, J. K. Assessing the Reliability of Calculated Catalytic Ammonia Synthesis Rates. *Science (80-.).* **2014**, *345* (6193), 197–200. https://doi.org/10.1126/science.1253486.

(61)   Lamoureux, P. S.; Singh, A. R.; Chan, K. PH Effects on Hydrogen Evolution and Oxidation over Pt(111): Insights from First-Principles. *ACS Catal.* **2019**, *9* (7), 6194–6201. https://doi.org/10.1021/acscatal.9b00268.

(62)   Trasatti, S. International Union Of Pure And Applied Chemistry Commission On Electrochemistry * The Absolute Electrode Potential : An Explanatory Note. **1986**, *58* (7), 955–966.

(63)   Medford, A. J.; Shi, C.; Hoffmann, M. J.; Lausche, A. C.; Fitzgibbon, S. R.; Bligaard, T.; Nørskov, J. K. CatMAP: A Software Package for Descriptor-Based Microkinetic Mapping of Catalytic Trends. *Catal. Letters* **2015**, *145* (3), 794–807. https://doi.org/10.1007/s10562-015-1495-6.

(64)   Heenen, H. H.; Kastlunger, G.; Shin, H.; Overa, S.; Joseph, A.; Jiao, F.; Chan, K. Mechanism for Acetate Formation in CO(2) Reduction on Cu : Selectivity Trends with PH and Nanostructuring Derive from Mass Transport. *ChemRxiv* **2021**, No. This content is a preprint and has not been peer-reviewed., DOI:10.33774/chemrxiv-2021-p3d4s. https://doi.org/10.33774/chemrxiv-2021-p3d4s.

(65)   Damaskin, B. B.; Baturina, O. A.; Stenina, E. V.; Sviridova, L. N. Specific Adsorption of Anions on a Copper (100) Single Crystal Electrode Studied by Charge Displacement by CO Adsorption and Infrared Spectroscopy. *Electrochim. Acta* **2001**, *46* (20–21), 3083–3090. https://doi.org/10.1016/S0013-4686(01)00599-0.

(66)   Resasco, J.; Lum, Y.; Clark, E.; Zeledon, J. Z.; Bell, A. T. Effects of Anion Identity and Concentration on Electrochemical Reduction of CO 2. *ChemElectroChem* **2018**, *5* (7), 1064–1072. https://doi.org/10.1002/celc.201701316.

(67)   Wuttig, A.; Ryu, J.; Surendranath, Y. Electrolyte Competition Controls Surface Binding of CO Intermediates to CO 2 Reduction Catalysts. *J. Phys. Chem. C* **2021**, *125* (31), 17042–17050. https://doi.org/10.1021/acs.jpcc.1c04337.

(68)   Resasco, J.; Bell, A. T. Electrocatalytic CO2 Reduction to Fuels: Progress and Opportunities. *Trends Chem.* **2020**, *2* (9), 825–836. https://doi.org/10.1016/j.trechm.2020.06.007.

(69)   Lee, S. H.; Lin, J. C.; Farmand, M.; Landers, A. T.; Feaster, J. T.; Avilés Acosta, J. E.; Beeman, J. W.; Ye, Y.; Yano, J.; Mehta, A.; Davis, R. C.; Jaramillo, T. F.; Hahn, C.; Drisdell, W. S. Oxidation State and Surface Reconstruction of Cu under CO 2 Reduction Conditions from In Situ X-Ray Characterization. *J. Am. Chem. Soc.* **2021**, *143* (2), 588–592. https://doi.org/10.1021/jacs.0c10017.

(70)   Magnussen, O. M.; Groß, A. Toward an Atomic-Scale Understanding of Electrochemical Interface Structure and Dynamics. *J. Am. Chem. Soc.* **2019**, *141* (12), 4777–4790. https://doi.org/10.1021/jacs.8b13188.

(71)   Pérez-Gallent, E.; Marcandalli, G.; Figueiredo, M. C.; Calle-Vallejo, F.; Koper, M. T. M. Structure- and Potential-Dependent Cation Effects on CO Reduction at Copper Single-Crystal Electrodes. *J. Am. Chem. Soc.* **2017**, *139* (45), 16412–16419. https://doi.org/10.1021/jacs.7b10142.

(72)   Gauthier, J. A.; Dickens, C. F.; Ringe, S.; Chan, K. Practical Considerations for Continuum Models Applied to Surface Electrochemistry. *ChemPhysChem* **2019**, *20* (22), 3074–3080. https://doi.org/10.1002/cphc.201900536.

(73)   Gauthier, J. A.; Ringe, S.; Dickens, C. F.; Garza, A. J.; Bell, A. T.; Head-Gordon, M.; Nørskov, J. K.; Chan, K. Challenges in Modeling Electrochemical Reaction Energetics with Polarizable Continuum Models. *ACS Catal.* **2019**, *9* (2), 920–931. https://doi.org/10.1021/acscatal.8b02793.

(74)   Gauthier, J. A.; Dickens, C. F.; Heenen, H. H.; Vijay, S.; Ringe, S.; Chan, K. Unified Approach to Implicit and Explicit Solvent Simulations of Electrochemical Reaction Energetics. *J. Chem. Theory Comput.* **2019**, *15* (12), 6895–6906. https://doi.org/10.1021/acs.jctc.9b00717.

(75)   Schmidt, U. The Solubility of Carbon Monoxide and Hydrogen in Water and Sea-Water at Partial Pressures of about 10 -5 Atmospheres. *Tellus* **1979**, *31* (1), 68–74. https://doi.org/10.3402/tellusa.v31i1.10411.

(76)   Wang, L.; Nitopi, S.; Wong, A. B.; Snider, J. L.; Nielander, A. C.; Morales-Guio, C. G.; Orazov, M.; Higgins, D. C.; Hahn, C.; Jaramillo, T. F. Electrochemically Converting Carbon Monoxide to Liquid Fuels by Directing Selectivity with Electrode Surface Area. *Nat. Catal.* **2019**, *2* (8), 702–708. https://doi.org/10.1038/s41929-019-0301-z.

(77)   Grosse, P.; Gao, D.; Scholten, F.; Sinev, I.; Mistry, H.; Roldan Cuenya, B. Dynamic Changes in the Structure, Chemical State and Catalytic Selectivity of Cu Nanocubes during CO 2 Electroreduction: Size and Support Effects. *Angew. Chemie Int. Ed.* **2018**, *57* (21), 6192–6197. https://doi.org/10.1002/anie.201802083.

(78)   Kim, Y.-G.; Baricuatro, J. H.; Javier, A.; Gregoire, J. M.; Soriaga, M. P. The Evolution of the Polycrystalline Copper Surface, First to Cu(111) and Then to Cu(100), at a Fixed CO 2 RR Potential: A Study by Operando EC-STM. *Langmuir* **2014**, *30* (50), 15053–15056. https://doi.org/10.1021/la504445g.

(79)   Lei, Q.; Zhu, H.; Song, K.; Wei, N.; Liu, L.; Zhang, D.; Yin, J.; Dong, X.; Yao, K.; Wang, N.; Li, X.; Davaasuren, B.; Wang, J.; Han, Y. Investigating the Origin of Enhanced C 2+ Selectivity in Oxide-/Hydroxide-Derived Copper Electrodes during CO 2 Electroreduction. *J. Am. Chem. Soc.* **2020**, *142* (9), 4213–4222. https://doi.org/10.1021/jacs.9b11790.

(80)   Clark, E. L.; Bell, A. T. Direct Observation of the Local Reaction Environment during the Electrochemical Reduction of CO 2. *J. Am. Chem. Soc.* **2018**, *140* (22), 7012–7020. https://doi.org/10.1021/jacs.8b04058.

(81)   Lobaccaro, P.; Mandal, L.; Motapothula, M. R.; Sherburne, M.; Martin, J.; Venkatesan, T.; Ager, J. W. Initial Application of Selected-Ion Flow-Tube Mass Spectrometry to Real-Time Product Detection in Electrochemical CO2 Reduction. *Energy Technol.* **2018**, *6* (1), 110–121. https://doi.org/10.1002/ENTE.201700628.

(82)   Khanipour, P.; Löffler, M.; Reichert, A. M.; Haase, F. T.; Mayrhofer, K. J. J.; Katsounaros, I. Electrochemical Real-Time Mass Spectrometry (EC-RTMS): Monitoring Electrochemical Reaction Products in Real Time. *Angew. Chemie - Int. Ed.* **2019**, *58* (22), 7273–7277. https://doi.org/10.1002/ANIE.201901923.

(83)   Li, C. W.; Ciston, J.; Kanan, M. W. Electroreduction of Carbon Monoxide to Liquid Fuel on Oxide-Derived Nanocrystalline Copper. *Nature* **2014**, *508* (7497), 504–507. https://doi.org/10.1038/nature13249.

(84)   Resasco, J.; Chen, L. D.; Clark, E.; Tsai, C.; Hahn, C.; Jaramillo, T. F.; Chan, K.; Bell, A. T. Promoter Effects of Alkali Metal Cations on the Electrochemical Reduction of Carbon Dioxide. *J. Am. Chem. Soc.* **2017**, *139* (32), 11277–11287. https://doi.org/10.1021/jacs.7b06765.